Eddy properties in the Western Mediterranean Sea from satellite altimetry and a numerical simulation

Romain Escudier, Lionel Renault, Ananda Pascual, Pierre Brasseur, Dudley Chelton

RESEARCH ARTICLE

Key Points:
- New HR simulation of the WMed returns realistic EKE levels, higher than altimetry estimates
- Three eddy detection methods are applied to altimetry maps and the simulation outputs
- In the region, eddies are small (20 km), short lived (median 13 days), and frequent (30/day)

Correspondence to:
R. Escudier,
rescudier@socib.es

Eddy properties in the Western Mediterranean Sea from satellite altimetry and a numerical simulation

Romain Escudier[1,2], Lionel Renault[3], Ananda Pascual[1], Pierre Brasseur[4], Dudley Chelton[5], and Jonathan Beuvier[6]

[1]IMEDEA, UIB-CSIC, Esporles, Spain, [2]SOCIB, Palma de Mallorca, Spain, [3]Department of Atmospheric and Oceanic Sciences, University of California, Los Angeles, California, USA, [4]CNRS, Laboratoire de Glaciologie et Géophysique de l'Environnement, Université de Grenoble, Grenoble, France, [5]College of Earth, Ocean, and Atmospheric Sciences, Oregon State University, Oregon, USA, [6]Mercator Ocean, Ramonville Saint-Agne, France

Abstract Three different eddy detection and tracking methods are applied to the outputs of a high-resolution simulation in the Western Mediterranean Sea in order to extract mesoscale eddy characteristics. The results are compared with the same eddy statistics derived from satellite altimetry maps over the same period. Eddy radii are around 30 km in altimetry maps whereas, in the model, they are around 20 km. This is probably due to the inability of altimetry maps to resolve the smaller mesoscale in the region. About 30 eddies are detected per day in the basin with a very heterogeneous spatial distribution and relatively short lifespans (median life around 13 days). Unlike other areas of the open ocean, they do not have a preferred direction of propagation but appear to be advected by mean currents. The number of detected eddies seems to present an annual cycle when separated according to their lifespan. With the numerical simulation, we show that anticyclones extend deeper in the water column and have a more conic shape than cyclones.

1. Introduction

Mesoscale eddies are omnipresent in the global ocean [*Chelton et al.*, 2011a] and play a key role in multiple ocean processes but are not yet fully analyzed and monitored at global scale due to their relatively small size. Unlike linear waves, nonlinear dynamics in mesoscale eddies can transport water mass with their heat content as well as chemical (e.g., salt) and biological properties (e.g., nutrients and biomass) over large distances. Their crucial role in the transport of heat fluxes has been shown in many studies [*Wunsch*, 1999; *Jayne and Marotzke*, 2002; *Colas et al.*, 2012], but the effect of eddy transport in the Mediterranean is still unknown. Concerning biology, apart from rotational advection within the eddy interior [*Chelton et al.*, 2011b; *Gaube et al.*, 2014] and the transport of biomass from one location to another [*Feng et al.*, 2007; *Llinás et al.*, 2009], mesoscale eddies modify the local mixed layer depth, significantly enhancing primary production [*Oschlies and Garçon*, 1998; *Levy et al.*, 1998; *Mahadevan et al.*, 2012]. Mesoscale eddies can also feed energy back to the main flow and drive large-scale circulation [*Lozier*, 1997; *Holland*, 1978], making them a key component of the ocean dynamics.

In the Western Mediterranean Sea (WMed), a high number of eddies have been observed and studied in the past with in situ observations [e.g., *Katz*, 1972; *Benzohra and Millot*, 1995; *Font et al.*, 1998; *Testor et al.*, 2005; *Hu et al.*, 2011; *Pascual et al.*, 2002; *Bouffard et al.*, 2010; *Amores et al.*, 2013]. Yet a systematic characterization of these eddies is still lacking due to the small scales involved in these processes in this region where the Rossby deformation radius that characterizes the horizontal scales of eddies is small (10–15 km) [*Beuvier et al.*, 2012a]. Such a systematic approach was only used in *Isern-Fontanet et al.* [2006] where an automated eddy detection applied to the first 7 years of altimetry data in the Mediterranean Sea and some results on the size, amplitude, and path of propagation of intense mesoscale eddies were obtained. Weaker eddies were not studied in details for being either altimetry maps errors or low energy states of intense eddies. The present study aims at the extension of these results with a longer time series, state-of-the-art methods and a numerical model for the western basin. A more recent study by *Mkhinini et al.* [2014] used an eddy detection method on 20 years of altimetry maps to study long-lived mesoscale eddies in the eastern basin. They showed an asymmetry between cyclones and anticyclones and then characterized long-lived eddy formation areas in the eastern basin. In the western basin, eddies present a wide range of different properties (size, shape, amplitude, duration, etc.) associated with different generating mechanisms (current instabilities,
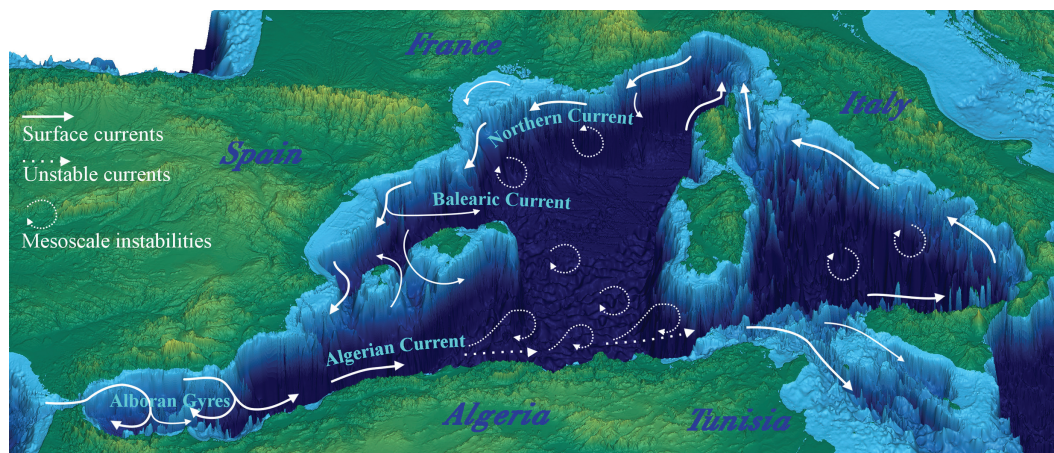
Figure 1. Area of study: the Western Mediterranean Sea. The map presents the bathymetry and the dynamical features. Adapted from *Millot* [1999].

wind forcing, and thermohaline fluxes) that are related to the complex coastline and bathymetry [*Malanotte-Rizzoli et al.*, 2013]. An overview of the mean surface circulation in the basin is shown in Figure 1.

The surface circulation in the Western Mediterranean Sea is mainly cyclonic around the basin with several areas where strong eddy activity has been observed. Along the Algerian shore, baroclinic instabilities of the Algerian Current generate meanders and, eventually, eddies that detach from the main current [*Olita et al.*, 2011]. With an extent that can reach more than 1000 m as observed by *Millot et al.* [1997] and *Ruiz et al.* [2002], these features have diameters of about 100–200 km and their lifetime ranges from several months up to 3 years [*Puillat et al.*, 2002].

In the northern part of the basin, the main current is the Northern Current, which flows westward along the French coast in the Ligurian Provençal Basin, the Gulf of Lion, and then along the Spanish coast in the Balearic Sea. Mesoscale activity has been observed in this region [*Robinson et al.*, 2001] with an increase in autumn [*Font et al.*, 1995]. Eddy formation there is hypothesized to be due to the combined effect of strong Tramontane winds and the Northern Current [*Millot*, 1982; *Hu et al.*, 2009; *Rubio et al.*, 2009].

When it arrives in the Balearic Sea, the Northern Current splits into two branches [*Font et al.*, 1988], one going back along the Balearic northern shore [*Ruiz et al.*, 2009; *Mason and Pascual*, 2013] and the other flowing southward through the Ibiza channel [*Pinot et al.*, 2002]. This circulation in the Balearic Sea is modulated by mesoscale activity that, at first, was underestimated [*La Violette et al.*, 1990] but later was found to be nonnegligible [*García et al.*, 1994]. In the Balearic Current, many studies have shown the existence of mesoscale structures by analyzing satellite data, drifting buoys, moorings, oceanographic cruises, or gliders [e.g., *Pinot et al.*, 1995; *Ruiz et al.*, 2009; *Bouffard et al.*, 2010, 2012]. The formation of such eddies has been hypothesized to be due to instabilities of the Balearic Current, the formation of a meander, and then a coherent vortex [*Amores et al.*, 2013] for the smaller eddies. Direct action of the wind can also transmit anticyclonic vorticity from the negative curl associated with the shear of the Mistral downstream of the Pyrenees, forming the larger eddies as proposed by *Pascual et al.* [2002] and *Mason and Pascual* [2013].

In this study, we apply eddy detection methods to a high-resolution model of the WMed and interpolated altimetry maps. The results allow us to extract some characteristics of mesoscale eddies in the area. The paper is organized as follows: in section 2, we describe the data sets used in the study and more particularly the high-resolution simulation of the WMed we developed for this study. In section 3, we present the eddy detection methods used. Then in section 4, the results and characteristics of the detected eddies are presented. Finally, in section 5, we discuss and summarize the results.

2. Sea Surface Height Data Sets

2.1. Altimetry Data
For comparison with the model simulation, gridded maps of absolute dynamic topography (ADT) from altimetry are obtained by interpolating along-track satellite data to obtain 2-D fields. In this study, we used
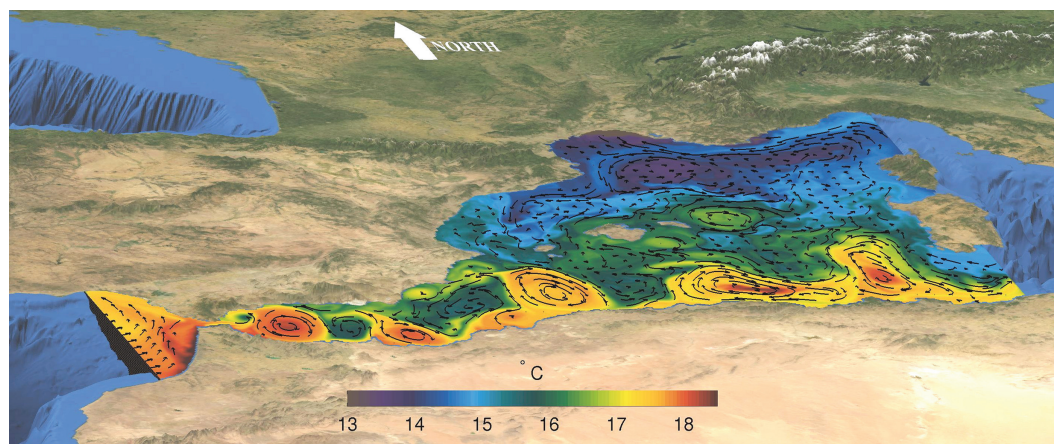
Figure 2. Snapshot of SST and surface currents of the simulation. This figure is for 1 December 2010.

daily, merged, delayed-time gridded maps of optimally interpolated sea level anomalies (SLA) provided by AVISO (http://www.aviso.oceanobs.com) for the period 1993–2012. This product is specially designed for the Mediterranean Sea [*Pujol and Larnicol*, 2005] on a higher-resolution grid (1/8°) than for the global data set. To generate these maps, all available satellites are used in the optimal interpolation (TOPEX/Poseidon, Jason-1/2, ERS 1/2, Envisat, and Geosat-Follow On [see *Pascual et al.*, 2007]). The along-track data from the satellites are filtered with a Lanczos filter to remove measurement noise (a half-power filter cutoff wavelength of 42 km) and then interpolated with a daily analysis. The spatial and temporal correlation scales are constant and set at 100 km and 10 days with a correlation function proposed by *Arhan and De Verdiere* [1985]. The optimal interpolation is set to correct long-wavelength errors and measurement noise. Details of the mapping procedure for the Mediterranean Sea can be found in *Pujol and Larnicol* [2005].

This data set will hereafter be called AVISOMED08.

2.2. High-Resolution Simulation of the Western Mediterranean Sea
2.2.1. Model Setup
The model used for this study is the Regional Ocean Modelling System (ROMS) [*Shchepetkin and McWilliams*, 2005; *Shchepetkin and McWilliams*, 2009] in its ROMS_AGRIF version [*Debreu et al.*, 2012]. The ROMS kernel is a 3-D free-surface, sigma-coordinate, split-explicit primitive equation model with Boussinesq and hydrostatic approximations. Its multiple-time-level time stepping and high-order upstream-biased advection schemes help to better resolve turbulent processes, while the sigma coordinates enable a good representation of complex bathymetry such as the Western Mediterranean Sea.

The domain covered by the simulation spans from the Gulf of Cádiz to Corsica and Sardinia (see Figure 2) and the period covers 1993–2012 with a 1 year spin-up (year 1992). The model grid is an Arakawa C-grid with 1/32° horizontal resolution and 32 terrain-following vertical levels with increased resolution in the upper levels. The horizontal resolution allows us to effectively resolve wavelengths over 24 km (corresponding to $7\Delta x$, as observed by *Marchesiello et al.* [2011]) which should be enough to represent eddies with radius over 6 km (one wavelength represent four radii). We used the recent vertical stretching function [*Shchepetkin and McWilliams*, 2009] with $\theta_S = 6.5$, $\theta_b = 1.5$, and $h_C = 250$ m. The surface and bottom control parameters (θ_S and θ_b) determine the stretching of the grid, and the critical depth (h_C) is the width of surface or bottom boundary layer in which higher vertical resolution is required during stretching.

The vertical diffusion scheme used is a nonlocal, K-profile planetary (KPP) boundary layer Large-McWilliams-Doney (LMD) scheme [*Large et al.*, 1994], which represents the unresolved physical vertical subgrid-scale processes.

We combined the bathymetry from *Smith and Sandwell* [1997] that covers the whole basin with a detailed bathymetry for the Gibraltar region [*Sanz*, 1991] that was filtered as in *Peliz et al.* [2012].

For the initial and boundary conditions, we used a part of a 55 year simulation performed with the NEM-OMED12 model over the 1958–2013 period; this simulation is described in *Beuvier et al.* [2012b].

Table 1. Characteristics of the ROMSWMED32 Simulation

Area	WMed: 7.4°W–10°E 34.6°N–44.7°N
Period	1993–2012
Horizontal resolution	1/32°
Forcings	NCEP-CFSR (6 h, 35 km)
Boundaries	NEMOMED12 (daily)
Sponge	Yes (45 km)
Nudging	2-D at boundaries
Outputs	Daily averages
Vertical levels: Number (θ_S, θ_B)	32 (6.5,1.5)
$r_{x0(max)}$	0.2
Δt	240 s
Nb barotropic steps	25
Background vertical mixing	0
Bottom drag	Linear ($\gamma = 0,0003$ m s^{-1})

NEMOMED12 covers the entire Mediterranean basin with a 1/12° horizontal resolution and provides a realistic initial state of the ocean and boundary conditions.

The atmospheric forcing is given by the NCEP-CFSR [*Saha et al.*, 2010] data set, which has a spatial grid of 35 km at a 6 h time step, using a bulk formulation [*Fairall et al.*, 2003] for the heat, momentum, and freshwater fluxes.

The river discharge is simulated as a freshwater input spread around the river mouths with the monthly climatology from *Dai et al.* [2009].

The characteristics of the simulation are summarized in Table 1. An example snapshot of the daily mean sea surface temperature (SST) and surface currents is presented in Figure 2. Various mesoscale eddies can be seen with a signature in SST as well as surface currents. The simulation will hereafter be called ROMSWMED32.

2.2.2. Evaluation of ROMSWMED32

Since this simulation is a new implementation of the ROMS model for the region, extensive validation has been performed. In this section, we will show two examples of the validation that are relevant for our study. The aim of the simulation is to be able to reproduce realistically the generation and propagation of surface mesoscale eddies.

First, we evaluate the simulation capabilities to reproduce the mean surface circulation of the Western Mediterranean Sea that is schematized in Figure 1. The mean ADT of the simulation over the whole time period (1993–2012) is shown in Figure 3, right. In this figure, we plotted also the mean dynamic topography (MDT) from *Rio et al.* [2014] with the added mean of SLA from altimetry (left). This MDT is constructed using an average of the outputs of an ocean model (the Mediterranean Forecasting System based on the NEMO code) as a first guess and adding the information of all of the available observations (drifters, CTD, and gliders) in the area. It represents the best estimate of the mean surface circulation that is currently available for the area. The corresponding geostrophic velocities are plotted on the two maps showing that the simulation performs very well in reproducing the main characteristics of the average circulation of the basin. The two Alboran gyres are well simulated, with the eastern one less intense due to its seasonality as described in *Renault et al.* [2012]. The main characteristics of the Algerian Current are well represented in the model, strong and narrow along the coast and unstable and weaker in the eastern part of the basin. The Northern Current is also well reproduced, as well as the Balearic Current.
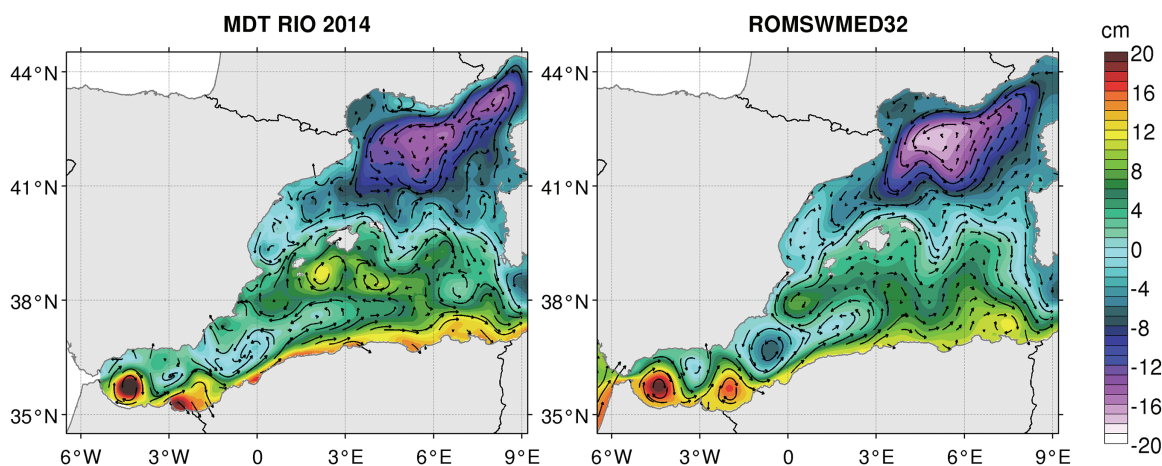
Figure 3. Mean ADT for the period 1992–2012 for the ROMSWMED32 simulation compared with the MDT from *Rio et al.* [2014]. Vectors are the geostrophic velocities computed from the respective ADT.
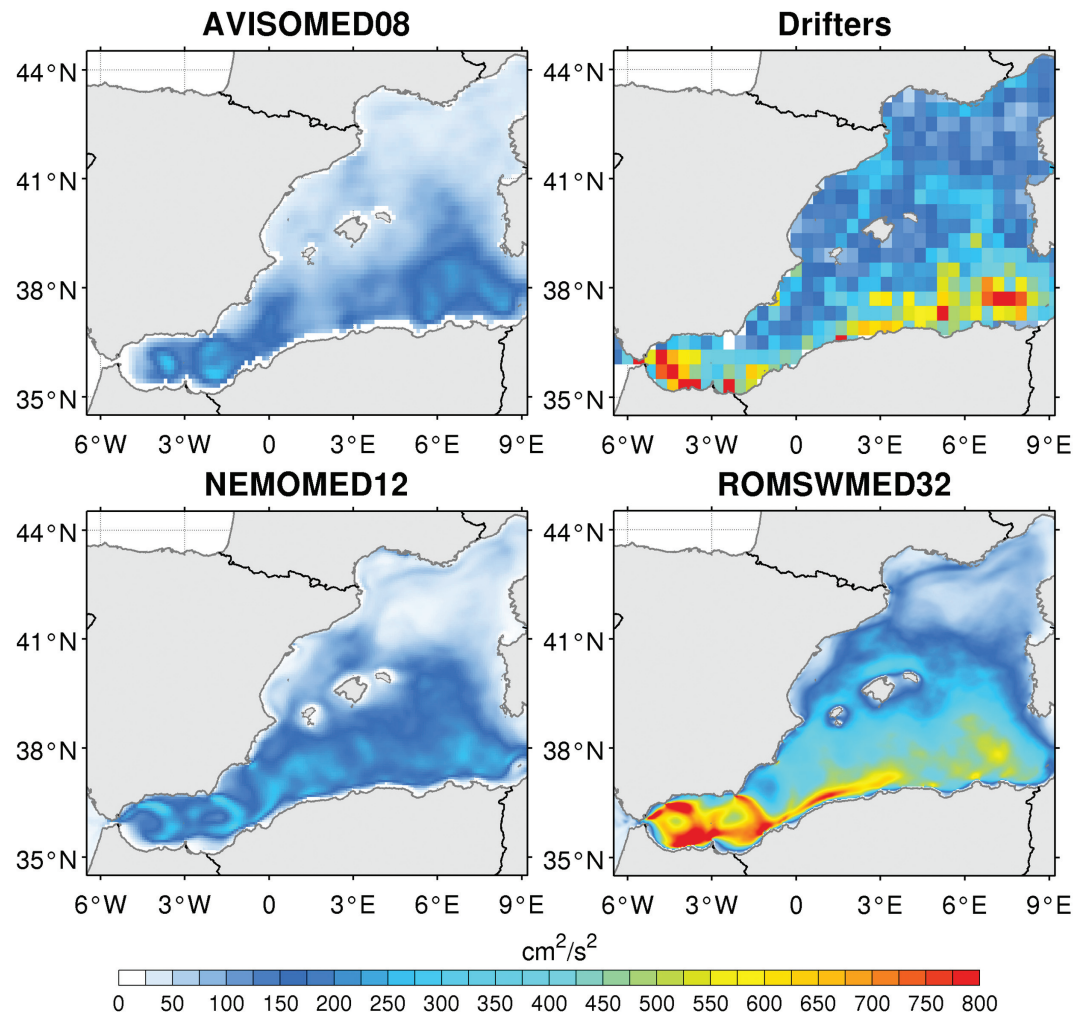
Figure 4. Comparison of mean EKE over the period 1992–2012 for (top left) AVISOMED08, (top right) drifter data, (bottom right) NEM-OMED12, and (bottom right) ROMSWMED32. Drifter data come from the database compiled by *Poulain et al.* [2012].

The eddy kinetic energy (EKE) is defined as the kinetic energy (KE) that is due to transient dynamics and is given by:

$$EKE = \frac{1}{2}\left((u-\bar{u})^2 + (v-\bar{v})^2\right) \tag{1}$$

with u, v the instantaneous currents, $\bar{u}$ and $\bar{v}$ the mean currents over the whole 1993–2012 period. Figure 4 shows the mean EKE computed from geostrophic velocities u_g and v_g estimated from altimetry maps, drifters trajectories, the coarser mother-simulation NEMOMED12, and the ROMSWMED32 simulation. For the two models, we used the SSH output to estimate the geostrophic velocities. Velocities of drifters are edited to remove outliers, interpolated, filtered at 36 h to remove high-frequency oscillations and subsampled. Ekman currents are not removed in this estimation but a sensitivity test in a smaller area showed no significant change in the EKE after removing Ekman currents. The EKE is estimated from the drifters by taking the mean velocities within boxes of $1/3° \times 1/3°$ and computing anomalies of velocities with respect to this mean.

Although the levels of EKE in Figure 4 are quite different between the data sets, the geographical distributions are similar. The regions with high EKE are the ones identified in the introduction as having high meso-scale activity. Strong EKE levels are found at the locations of strong KE levels associated with mean currents, suggesting that the principal origins for these eddies are baroclinic or barotropic instabilities of the perma-nent currents. EKE computed from AVISOMED08 (altimetry maps) is much weaker (by more than a factor of 2) than EKE from drifters. The drifters may overestimate the energy due to residual wind-driven and
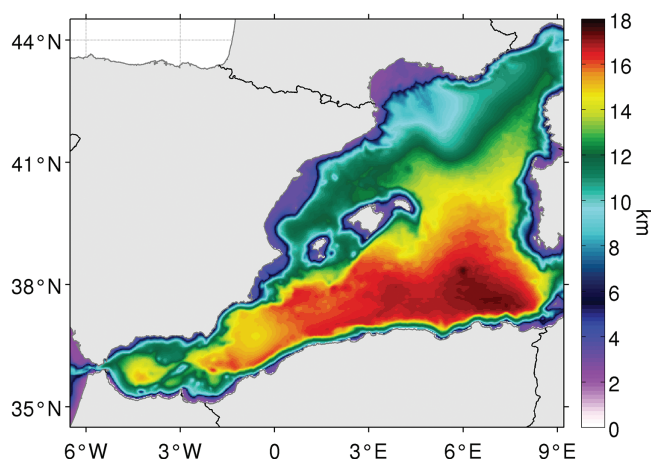
Figure 5. Map of the Rossby first radius of deformation in the region computed from the 20 years average of the ROMSWMED32 simulation. The radius has been estimated using the WKB approximation [see *Chelton et al.*, 1998].

nongeostrophic currents [*Poulain et al.*, 2012], but this is not likely sufficient to explain such a discrepancy. The levels of EKE in NEMOMED12 are also weaker, close to the values of altimetry, but the ROMSWMED32 simulation gives energy values that are more consistent with drifters estimates.

Altimetry gridded fields (and NEMOMED12) clearly underestimate the energy of mesoscale dynamics in the region. This might be attributable to the inability of gridded altimetry to resolve wavelength scales shorter than about 100 km while ROMSWMED32 is able to resolve scales down to 24 km in wavelength (for 1/32° grid resolution). New techniques of optimal interpolation have been developed to improve the altimetry product such as *Dussurget et al.* [2011] and, in the WMed, *Escudier et al.* [2013]. The improvement of the method described in *Escudier et al.* [2013] is useful for specific cases near the overpass of a satellite and do not resolve the fundamental limitation of altimetry which is the distance between neighboring ground tracks (see also *Bouffard et al.* [2014] for a discussion on this). The new fields provided by this method have an increased EKE but still much smaller than the simulation or drifters.

To confirm the relevance of the model resolution, we present on Figure 5 an estimation of the value of the Rossby first radius of deformation in the area using the ROMSWMED32 simulation. This map shows that we have indeed short scales (10–15 km) in the region with shorter scales in the northern part (8–12 km). With a feature wavelength resolution of 24 km, the simulation should be able to resolve structures with radii of around 6 km, which is sufficient in most of the domain.

Other validations with observations have been performed such as comparisons with transports, water masses, sea surface temperature from satellites, or deep water convection. The Gibraltar Strait transport, a key feature for the circulation in the Mediterranean, is in average 0.87 Sv for the inflow and 0.53 Sv for the outflow, which is comparable to observation estimates (0.82 Sv inflow and 0.78 Sv outflow [*Criado-Aldeanueva et al.*, 2012]) for the inflow and weaker for the outflow, probably due to the smoothed and therefore shallower bathymetry in Gibraltar. The details of these validations can be found in *Escudier* [2015] (http://www.tdx.cat/handle/10803/310417 or https://tel.archives-ouvertes.fr/tel-01172378). These metrics and the rest of our validation give us confidence in the ROMSWMED32 simulation capabilities to simulate mesoscale activity in the WMed.

3. Eddy Detection Methods

3.1. Closed Contours of SLA

The first method used to detect and track eddies in the data sets is the one developed by *Chelton et al.* [2011a]. This approach consists of detecting closed contours of SLA that include a local extremum and several other criteria, to identify and track mesoscale eddies. In this method, an eddy is viewed as a coherent isolated vortex and therefore the corresponding SLA has the form of a bump or a depression. A detailed description of the method can be found in *Chelton et al.* [2011a].

This method was successfully applied to the global ocean and the global data set is available at http://cioss.coas.oregonstate.edu/eddies/. A preliminary study of the results of this eddy detection and tracking method when applied to the Mediterranean Sea revealed that the method needed some adjustments to adapt to the small amplitudes and scales of the eddies in this region. Several issues were identified and modifications were applied to the algorithm to obtain a more reliable data set. The modifications included the change of the parameters (upper bound of 800 pixels, sea level increment of 0.5 cm for the search, 200 km

for the intra-eddy length scale), interpolation to a finer grid, an extrapolation to the coast, the use of daily maps and the removal of eddies with irregular shapes.

This method will be referred to hereafter as the CHE11 method.

3.2. Geometry of Velocities

The second method used to detect and track eddies in the WMed is based on the geometry of surface velocities. Its objective is to detect a region where the velocity field rotates around a center. The description of the algorithm and its application can be found in *Nencioli et al.* [2010]. Since we are comparing this method with others that rely on SLA and we want to apply it to altimetry maps, the velocities used in this study are geostrophic velocities computed from the SLA with the equation for geostrophic equilibrium:

$$u_g = -\frac{g}{f} \cdot \frac{\partial \eta}{\partial y} \tag{2}$$

$$v_g = \frac{g}{f} \cdot \frac{\partial \eta}{\partial x} \tag{3}$$

with g the acceleration of gravity, f the Coriolis parameter, and η the SLA. The discretization of the equations is done with a three-point centered difference scheme.

This method will be referred to hereafter as the NEN10 method.

3.3. Combination of Okubo-Weiss Parameter and Closed Contours

The third method employed is the one described by *Halo et al.* [2013]. This method combines the geometric criteria similar to CHE11 and traditional methods [e.g., *Isern-Fontanet et al.*, 2006; *Chelton et al.*, 2007; *Penven et al.*, 2005] based on local deformation properties of the flow such as the Okubo-Weiss parameter. The Okubo-Weiss [*Okubo*, 1970; *Weiss*, 1991] parameter is defined as:

$$W = S_n^2 + S_s^2 - \zeta^2 \qquad \text{with} \qquad \begin{cases} S_n = \dfrac{\partial u}{\partial x} - \dfrac{\partial v}{\partial y} \\[1mm] S_s = \dfrac{\partial v}{\partial x} + \dfrac{\partial u}{\partial y} \\[1mm] \zeta = \dfrac{\partial v}{\partial x} - \dfrac{\partial u}{\partial y} \end{cases} \tag{4}$$

where S_n and S_s are the normal and shear components of the strain and ζ, the relative vorticity. In this method, a geostrophic or mesoscale eddy is contained within a closed contour of SLA and dominated by vorticity ($W < 0$).

This method will be referred to hereafter as the HAL13 method.

3.4. Qualitative Comparisons Between the Different Methods

Many methods exist to automatically detect and track eddies. The methods presented here have been chosen because they have different approach and represent the existing standard methods. An example of the results of the three eddy detection methods applied to the output of the simulation is presented in Figure 6. This figure highlights the difficulty of the development of an automated eddy detection algorithm for the WMed. While agreeing on a fair number of eddies (in this example, 44 eddies are detected by at least two methods and only 4 eddies are detected by one single method), the three methods give different results for the shapes and locations of the detected eddies. This is due to the difficulty of the eddy detection in this region where the coastline, bathymetry, and circulation are complex and the methods rely on different criteria. No method appears to stand out as superior to the others and we therefore decided to use all three methods. The three methods are applied to the data sets and then only the results and conclusion that are consistent between all three methods are considered and presented to assure their robustness.

4. Eddy Kinematic Properties

4.1. Intrinsic Characteristics

To assess the validity of the results of the eddy detection and tracking methods, we look at the distribution of eddies according to their size for the three methods applied to both gridded altimetry data and the
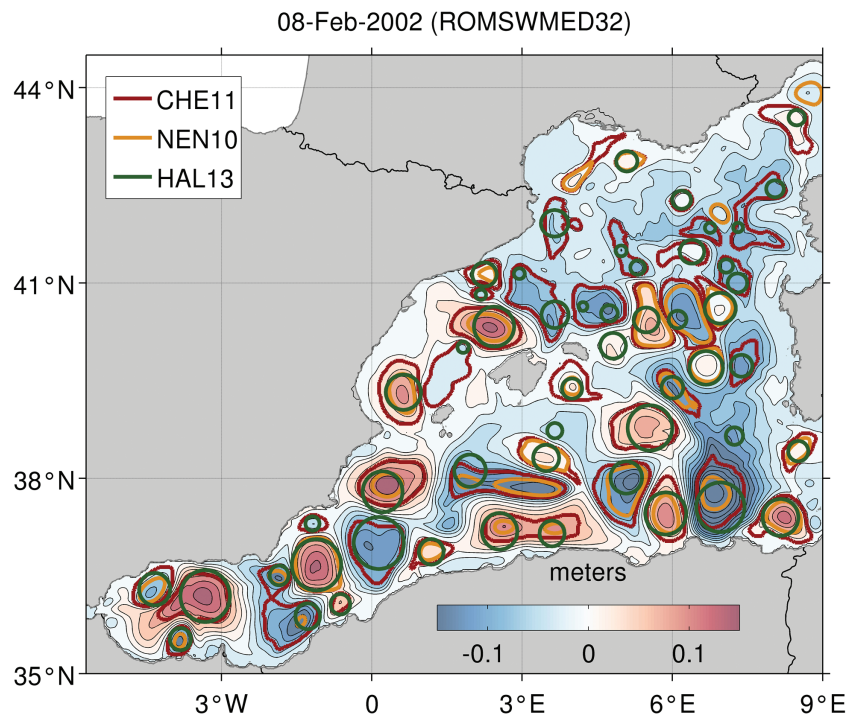
Figure 6. SLA output from ROMSWMED32 for 8 February 2002. The colors show the shapes of eddies detected by the three different methods. For HAL13, the detection method does not provide a shape, and a circle of the detected radius is plotted instead.

output of the ROMSWMED32 simulation (Figure 7). The distribution of the radii obtained by the different methods differs significantly. For all methods, the eddy radius is defined as an effective radius: $R = \sqrt{S/\pi}$ with S the surface of the shape detected by the algorithm. The eddy radii from the NEN10 method are always smaller, which is related to the way the shapes of the eddies are defined. Looking at instantaneous maps (see for example Figure 6), we can see that the eddies are mostly in the same locations as in other methods but the areas in the eddy interiors are systematically smaller. The CHE11 method detected a higher number of large eddies than the other two methods, also highlighting differences in the detection of shapes.

With all three algorithms, there are more small detected eddies in the model (ROMSWMED32) than in the altimetry data set (AVISOMED08). For the altimetry product, the detected eddies are found to have peaks of the distributions of the radii around 30 km with both CHE11 and HAL13 and 20 km with NEN10, while for ROMSWMED32, the peaks of the distributions are between 20 and 25 km. The smaller scales of the eddies in the model are associated with a large increase in the number of detected eddies (more than twice as many), which is presumably related to the ability of the simulation to resolve smaller scales than altimetry maps as noted in section 2.

In Figure 7 (bottom), the upper-tail cumulative distribution of the lifetimes of eddies is plotted. The cumulative percentage of detected eddies decreases rapidly, with half of the eddies having a lifespan shorter than 13 days. The algorithms give somewhat different results but the shapes of the distributions are similar and there are more long-lived eddies in the ROMSWMED32 simulation. This is again likely due to the better performance of tracking algorithms in the simulation. The simulation has a 1 day time step which makes it easier for the algorithms to track the eddies. The altimetry tracks are interpolated to obtain daily maps but without satellite data every day. Moreover, because of limitations in the resolution capability of the altimeter data set (section 2), eddies can become temporarily "lost" in the poorly sampled regions and then reappear later when the altimeter coverage improves. In such cases, a single propagating eddy with a long lifetime would be identified as multiple eddies with shorter lifetimes. Except when noted, all subsequent plots in this study will be made arbitrarily with the CHE11 method for clarity, but all the results presented here are consistent between the methods [*Escudier*, 2015] and any other method could have been chosen.

The spatial distribution of large eddies is similar to the one for long-lived eddies (see next section), which suggests that there may be a correlation between radius and duration of the eddies. To investigate this
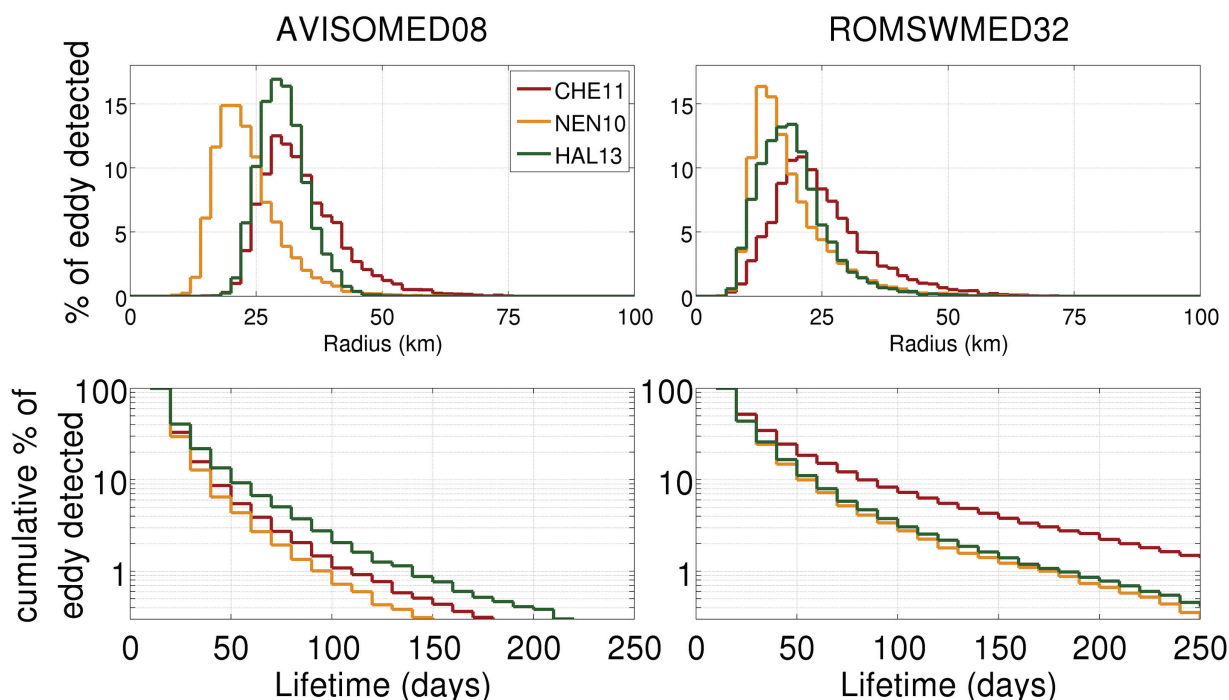
Figure 7. Distribution of the detected eddies according to (first row) radial scale and (second row) lifetime for (left column) AVISOMED08 (altimetry) and (right column) ROMSWMED32.

relationship, we separate the eddies into different classes of duration: 7–25, 25–50, 50–100, 100–150, 150–200, and 200–250 days. We then compute the evolution of the average radius for the eddies of each class with respect to the dimensionless age $t' = (t-1)/T$ with T the lifespan of the eddy and t its age. This evolution is plotted in Figure 8 and, for clarity, the dimensionless axis is multiplied for each class by the median of the lifespan (e.g., 75 for the 50–100 day class). The results confirm that the longer-lived eddies tend to have larger radii as seen in both altimetry data and model. It appears that, on average, eddies grow in size for the first part of their life history, then stabilize at their maximum size and, at the end, the eddy radius decreases rapidly before collapsing. For eddies with lifetime shorter than 150 days, these results stand out clearly. For longer-lived eddies, while it is also the case in the model, and with altimetry maps, there are too few eddies to draw any conclusion but it is likely safe to extrapolate that the results should be similar. This is consistent with the results obtained by *Samelson et al.* [2014] for the global ocean.

4.2. Spatial Distribution

We can also study the spatial distribution of the detected eddy centroids for the whole 1993–2012 period. Figure 9 confirms that many more eddies are detected in the high-resolution simulation than in altimetry maps. Yet the areas where most eddies are found are similar when compared with altimetry observations, at least in the southern part of the domain: the Alboran Sea, the Algerian Current, the center of the basin, and the Balearic Sea. For the Algerian Current, a seesaw pattern appears in the altimetry map that is likely attributable to the sampling tracks of satellite altimeters.

Significant differences between the model and altimetry maps occur along the Northern Current where many eddies are detected in the simulation but very few in the altimetry maps. Part of the reason for this discrepancy is explored in Figure 10, which shows that, in the simulation, there is a clear North-South difference in term of eddy radius, with smaller eddies detected in the northern part of the basin. This difference is likely related to the Rossby deformation radius, which is also reduced in the northern part (see Figure 5). The North-South difference does not appear for altimetry data where the smaller eddies in the northern region are not detected in the altimetry maps due to the limited resolution of the product (see section 2). This explains why altimetry maps exhibit less eddies in the Northern region than the simulation which resolves higher spatial scales.

The direction and speed of propagation of the detected eddies are presented in Figure 11. The propagation speed of the detected eddies is quite small, with most of the eddies moving at speeds below 8 cm s^{-1} in all
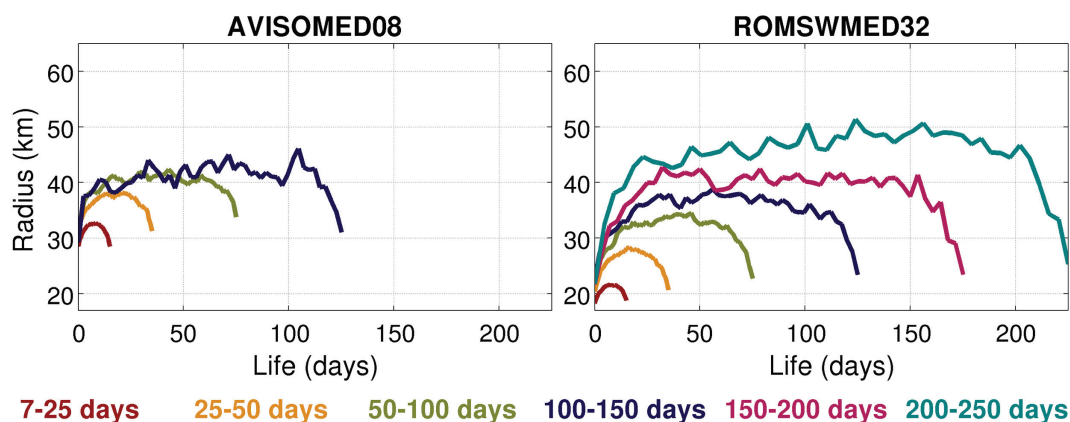
Figure 8. Evolution of eddy radii as a function of their age by lifespan class. The curves are computed with averages of at least 20 eddies.

the regions. This is consistent with previous observations of mesoscale eddies in the region [*Puillat et al.*, 2002; *Isern-Fontanet et al.*, 2006].

Over the whole WMed basin, there is generally east-west preference in the propagation of eddies in altimetry data, with a slight rotation of around 15° toward northeast-southwest propagation in the simulation. This inclination may be due to the geometry of the basin associated with the soutwest to northeast orientation of the Spanish and French coast and the larger number of detected eddies in this region for the simulation.

In the southern part of the basin (the Algerian region, second column in Figure 11), satellite-detected eddies have a clear tendency to go eastward with the Algerian Current. This is also strongly pronounced in the ROMSWMED32 simulation but with greater speeds.

In the northern region, the Northern Current appears to advect eddies, resulting in a westward (with a small southward inclination) propagation of the mesoscale structures in both altimetry data and the model. The westward preference is stronger and the inclination southward is more pronounced in the model.

The central region is interesting for the AVISOMED08 data set in which the results are similar to the generally westward propagation found for the global ocean [*Chelton et al.*, 2011a]. In this area with weak currents, this corresponds to the westward propagation of an isolated vortex [*McWilliams and Flierl*, 1979]. However, in ROMSWMED32, the directions are both westward and eastward with only a weak preference for westward propagation.
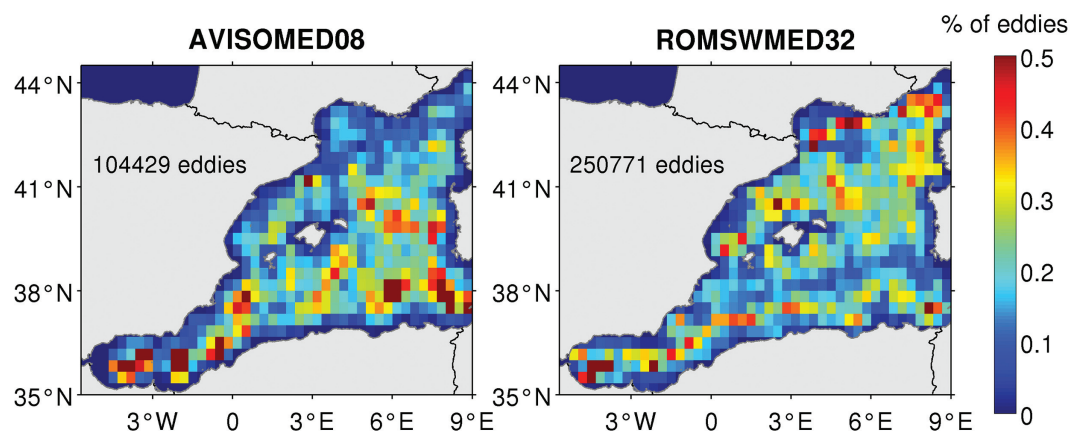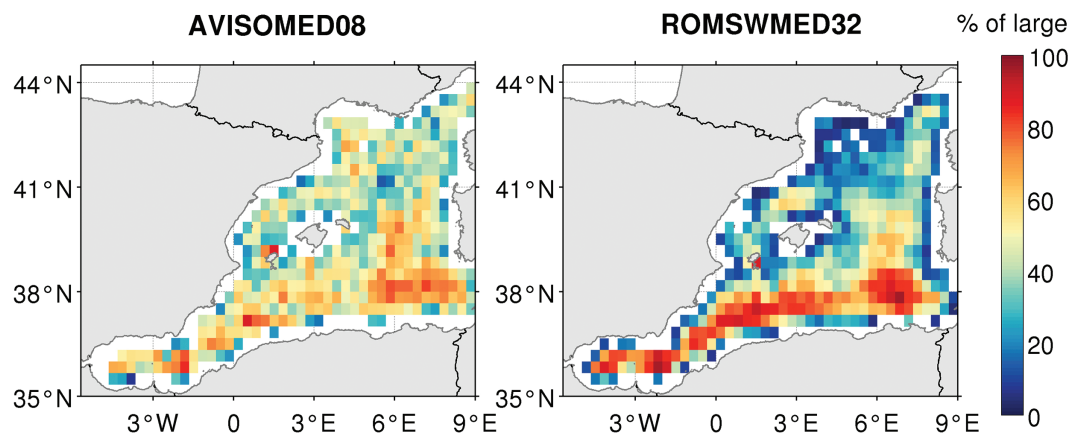

Figure 9. Percentage of detected eddies in each cell of 1/3° × 1/3° of the domain for both data sets. Each eddy is counted in the cell that contains its centroid on each day it is detected.

Figure 10. Spatial distribution of the percentage of large eddies (radius larger than 35 km). Cells with less than 20 eddies have been removed.

4.3. Temporal Evolution

The mean number of eddies detected per day for the whole period is around 15 for altimetry and more than twice that (34) for ROMSWMED32. The standard deviation is also twice as large for the model as for the altimetry maps. An annual cycle is apparent in the model time series of the number of eddies detected per day, whereas for altimetry maps, no annual cycle seems to be present.

Computed spectra of the time series of the number of detected eddies are shown in Figure 12. They confirm that the simulation of the WMed has a clear annual cycle, while in the altimetry data, the peak at the frequency equivalent to the annual cycle is not significant. The same results are found from all three eddy detection methods.

To investigate annual variability in the model and the altimetry data, the climatologies of the detected eddy number of eddies are presented in Figure 13. In this figure, long-lived and short-lived eddies are presented separately. This shows that there is an annual cycle in the altimetry data for both subsets but they are in opposite phases with similar amplitude. The two cycles thus compensate in the total number of detected
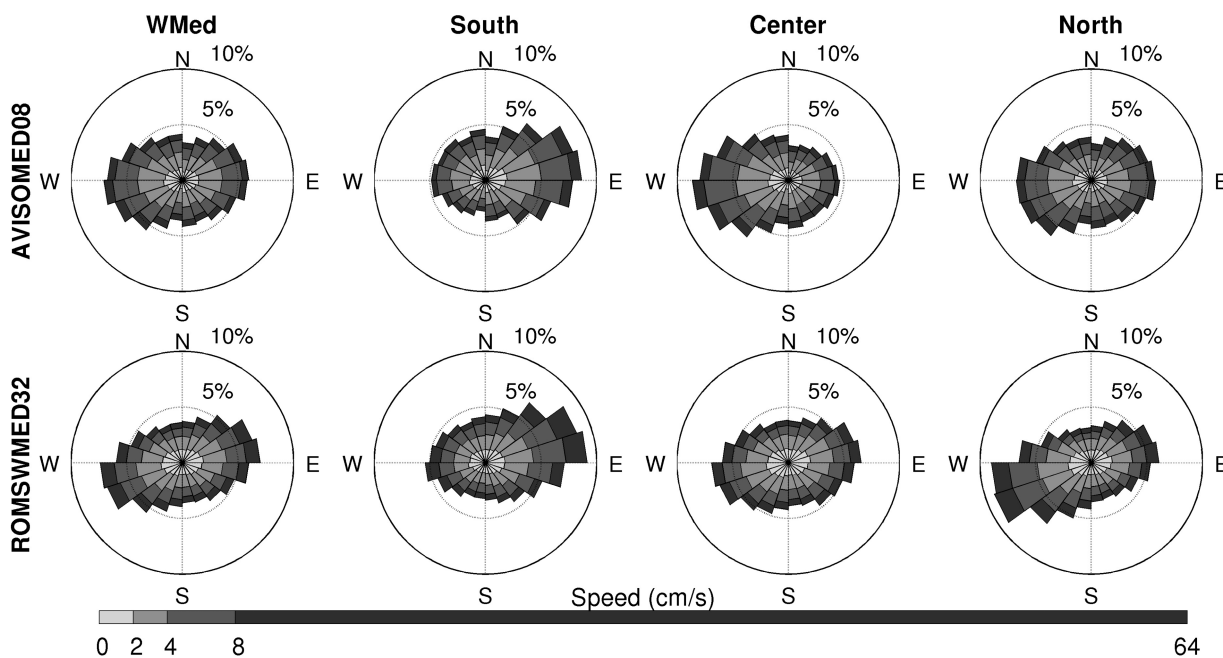
Figure 11. Polar histogram of the direction of propagation of the detected eddies in (top) AVISOMED08 and (bottom) ROMSWMED32. In grey shade is the distribution of velocities in each direction. The WMed is separated in three different regions: south (Algerian basins), center (Algero-Provençal basin), and north (Gulf of Lion and Balearic Sea).
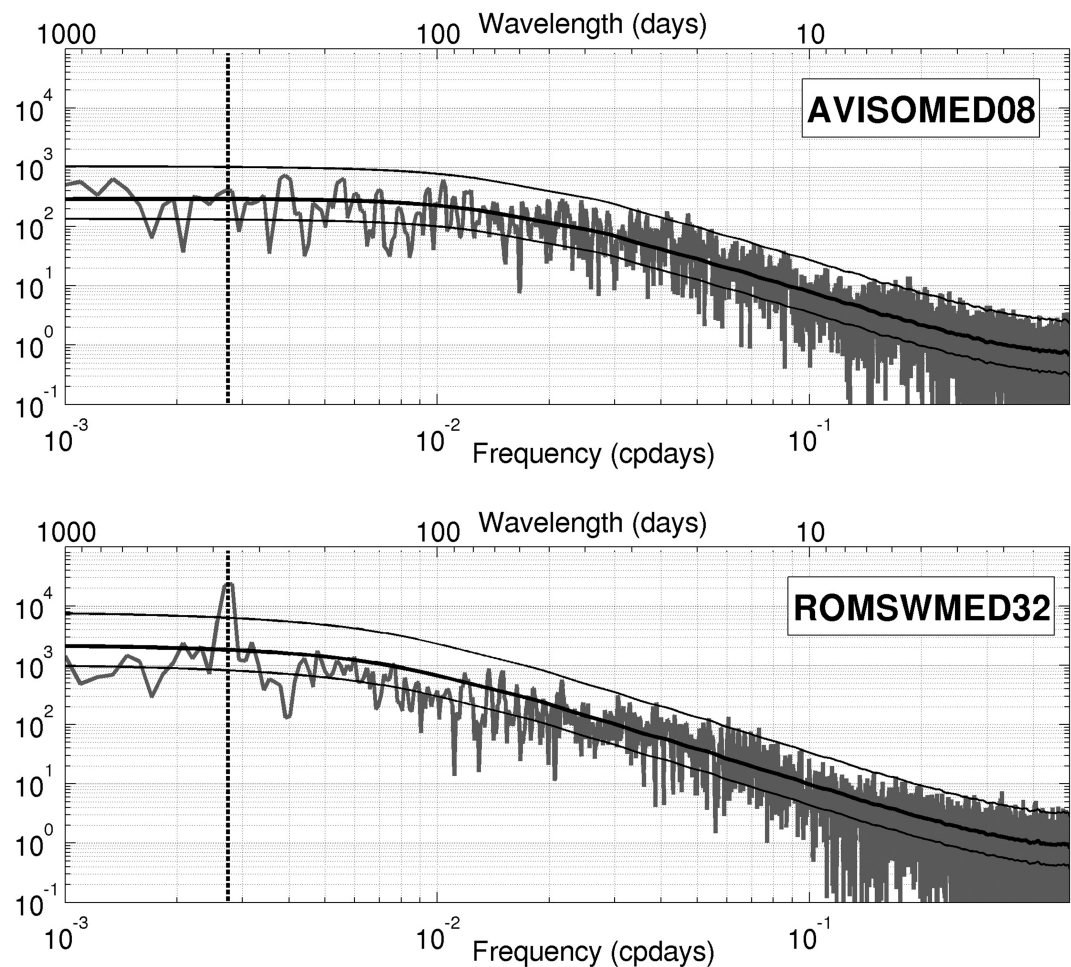
Figure 12. Power spectra of the time series of the number of detected eddies for the (top) AVISOMED08 and (bottom) ROMSWMED32 in grey. The fitted red noise with the corresponding confidence intervals is plotted as the black line. The vertical dashed line corresponds to the 1 year frequency.

eddies. In the numerical simulation, there is, like in altimetry maps, more short-lived eddies in spring but the number of long-lived eddies also peaks in late spring and therefore the cycles do not compensate. This explains why there is a signal at the annual frequency in the spectra for the simulation. The difference between the two data sets might be related to the eddy tracking that is easier in the simulation, which results in the much higher number of long-lived eddies (Figure 7).

4.4. Vertical Structure

The use of the numerical model provides information on the 3-D structure of the detected eddies. Composites of zonal cross sections through the centers of the eddies are shown in Figure 14. They are computed by taking the average of the zonal section of every eddy across its center. The density and velocity composites are calculated from anomalies with respect to the climatological values. To account for the variations of radii of the different eddies, the sections are taken as function of depth and a dimensionless distance from the center normalized by the computed radius of the eddy. As expected, cyclonic eddies induce negative anomalies of temperature and/or positive anomalies of salinity and therefore positive anomalies of density. This is because cyclones tend to uplift the pycnocline, thus raising colder, saltier water toward the sea surface. The effect is the opposite for anticyclonic eddies which lower the pycnocline. The anomalies extend horizontally to more than 1.5 times the detected radius.

The composite sections of meridional velocities confirm the rotation direction of the two type of eddies. They also show that the radius detected by the detection method is not exactly where the velocities are
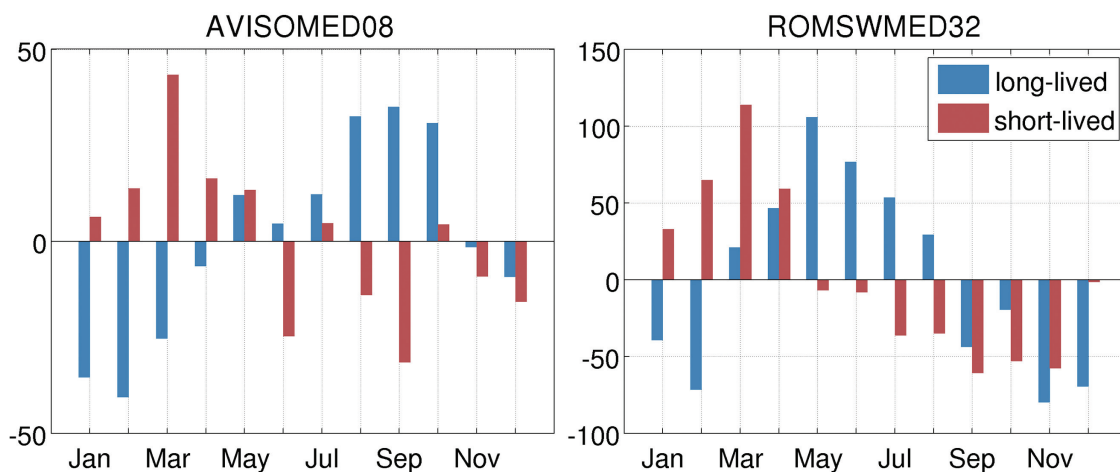
Figure 13. Climatology of the number of detected eddies for (left) altimetry observations and (right) the numerical model. Eddies are separated into two categories, eddies that live longer than 4 weeks (long lived) and eddies that live shorter than 4 weeks (short lived). The mean number of eddies detected per month for each data set has been removed to the climatology for clarity. For AVISOMED08, this value is 139 for long-lived and 288 for short-lived eddies. For ROMSWMED32, it is 648 for long-lived and 286 for short-lived eddies.

maximum for anticyclones but a little farther from the center (1.1 equivalent radius) which is surprising as the radius in this method is defined as the maximum rotation speed. This is due to a slight elongation of anticyclones in this region along the east-west direction. The same figure for north-south sections (not shown) shows that the maximum of velocities are closer than the equivalent radius. The Okubo-Weiss parameter defines the shape of the eddy since it is negative within it and positive outside. It shows that, on average, anticyclones extend deeper than cyclones. The shape of the vertical extension of the two types of eddies is also different. Anticyclones are smaller in radius at depth than at the surface which we can see clearly in the velocities where the maximum for each increasing depth is closer to the center. In the Okubo-
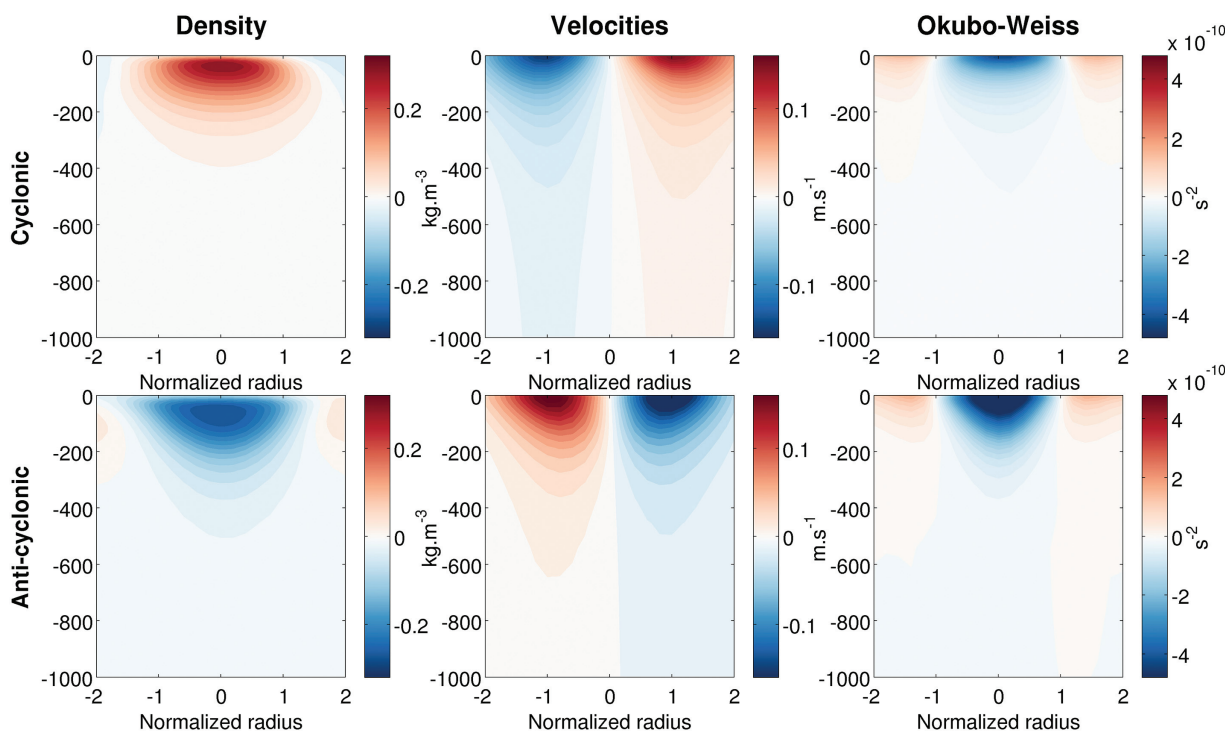
Figure 14. Composites of the zonal cross sections of the detected eddies for anomalies of density, meridional velocity, and the Okubo-Weiss parameter. The density and velocity composites are the mean of anomalies with respect to the climatology. Cyclones are shown in the first row and anticyclones in the second row. The *y* axis of the plots is the depth while the *x* axis is a dimensionless distance from the center.

Weiss parameter composites, it results in an almost triangular shape of the negative patch. For cyclones, the shape seems to be more cylindrical: the maxima of velocities for each depth are more or less at the same distance from the center and the negative Okubo-Weiss patch is more rectangular with smoothed edges.

5. Conclusions

5.1. Summary

The objective of this study was to characterize the properties of mesoscale eddies in the Western Mediterranean Sea. In this perspective, we developed a regional simulation of the region with the ROMS model (ROMSWMED32). The high horizontal spatial resolution (1/32°) enables the resolution of fine scales, and the long duration of the simulation (20 years: 1993–2012) makes the diagnostics robust and offers the possibility to look at some interannual variations (not discussed in this paper). The outputs of the final version of this new high-resolution simulation were validated by comparisons with observational data. EKE levels are higher in the numerical simulation, closer to observed levels in drifters, which points out the difficulties of altimetry to fully resolve mesoscale activity in the area because of the small eddy radii and resolution limitations of altimeter data.

We applied three eddy detection methods to the outputs of the ROMSWMED32 simulation and also altimetry gridded maps of SLA. These algorithms extract useful information (number, position, radial scale, and amplitude) of the eddies from the gridded fields. The results for the different detection and tracking methods exhibit some differences, highlighting the difficulty of studying mesoscale eddies in the region. However, the conclusions of this study were found to be robust to the different eddy identification procedures.

1. As expected, the number of detected eddies is higher for the high-resolution model (ROMSWMED32) than for the altimetry data set (from an average of 15 per day in AVISOMED08 to 34 in ROMSWMED32).
2. The mean radius of the detected structures decreases from about 30 km (AVISOMED08) to about 25 km (ROMSWMED32).
3. Most of the eddies have short lifespans; half of the eddies detected in the model or altimetry data had lifetimes shorter than 13 days.
4. The spatial distribution of the number of detected eddies is highly nonuniform and follows well-defined patterns that are consistent between the data sets and are likely a consequence of eddy formation processes.
5. A temporal analysis of the number of detected eddies per day reveals that there are different seasonal cycles in both of the data sets for long-lived (more than 4 weeks) and for short-lived (less than 4 weeks) eddies. A more in-depth study of this phenomenon will be conducted in the future.
6. The trajectories of detected eddies seem to follow the main currents of the region.
7. The relationship between the size of an eddy and its duration was also examined. Results show that, on average, the radial scale of an eddy increases and reaches a stabilized phase of relatively constant size before decreasing and finally collapsing. Long-lived eddies tend to grow more rapidly toward bigger size.
8. Composites of the vertical structures of the eddies in the ROMSWMED32 simulation show that anticyclones have a more conic shape than cyclones.
9. Mesoscale eddies in the region have an elongated shape along the east-west direction.

5.2. Discussion

In this study, we showed that mesoscale dynamics are energetic in the WMed while the horizontal scales of these structures are small due to a small Rossby radius. Therefore, the need for higher spatial resolution observations is stressed. This could be addressed with a higher density of satellite altimeters but also the synergy with fine grid in situ data such as coastal radar or gliders. The launch of the satellite SWOT with an expected spatial resolution of 10–25 km in wavelength will also hopefully increase our observational knowledge of fine mesoscale variability in this region [*Fu et al.*, 2009].

The observation data can be complemented with the use of numerical modeling. We showed that computational capabilities are now sufficient to simulate mesoscale activity with energy levels similar to what is observed in our area of study. Still, it might be beneficial to increase the resolution even more to represent the finer scales that could reach 5–10 km, which is the Rossby radius in some areas of the region. A future

study should be conducted to determine the model resolution that is most well suited for the study of mesoscale eddies in the region. The increase of resolution might only be needed in the northern part of the basin where the Rossby radius and therefore characteristic length scales are smaller.

Discrepancies between the model and the observations can also be partly due to the lack of parameterization of the current feedback to the atmosphere in the model. The surface stress is estimated using the absolute wind and not the relative wind to the oceanic current. Some recent works show that the current effect on the surface stress can lead to a reduction of the EKE of the ocean via a "mechanical damping" [*Eden and Dietze*, 2009; *Renault et al.*, 2016] and hence a reduction of the wind work and even a negative geostrophic wind work inducing a deflection of energy from the ocean to the atmosphere [*Renault et al.*, 2016]. *Gaube et al.* [2015] and *Renault et al.* [2016] show the current-induced surface stress curl change induces a negative wind work and Ekman pumping velocities that are of the opposite sign to the surface vorticity of the eddy, inducing its attenuation and improving the realism of the simulation. However, *Renault et al.* [2016] shows uncoupled simulations that estimate the wind stress using the relative wind should use a parameterization of the wind response that partially reenergize the ocean, damping the eddy killing effect. Further specific studies over the Mediterranean Sea should assess to which extent the current feedback to the atmosphere damp the eddy kinetic energy and aim to characterize the atmospheric response.

Regarding the eddy detection methods, more effort is needed to assess which automatic detection and tracking algorithm is most robust. Improvement or combinations of existing methods could be undertaken to improve the detection results. Our approach of finding characteristics that are consistent between three different methods enabled the robust extraction of some properties of the eddies in the area. One other thing to note is that we used SLA rather than SSH/ADT for the detection of eddies. While this removes the uncertainty of the MDT in altimetry maps, it could introduce some differences when there is a permanent feature such as a gyre (e.g., Alboran Gyres). For our analysis, we removed the Alboran region when possible. The results presented here will be extended in the future to investigate, for example, the origin of the annual cycle in the model that was also found in short-lived eddies in altimetry data. Eddies in the different areas of the basin have different properties (radial scale, lifetime, and vertical structure) that may be linked to different formation processes, suggesting the need for an investigation of these processes. In particular, it would be interesting to study the influence of the wind, baroclinic instabilities and barotropic conversion, or the energy conversion that leads to the EKE [*Marchesiello et al.*, 2003]. Interannual variability has not been examined in this study and is left for a future study. To investigate the long-term evolution such as decadal variability, the 20 year run for this study could be extended.

References

Amores, A., S. Monserrat, and M. Marcos (2013), Vertical structure and temporal evolution of an anticyclonic eddy in the Balearic Sea (western Mediterranean), *J. Geophys. Res. Oceans*, *118*, 2097–2106, doi:10.1002/jgrc.20150.

Arhan, M., and A. C. De Verdiere (1985), Dynamics of eddy motions in the eastern north Atlantic, *J. Phys. Oceanogr.*, *15*(2), 153–170.

Benzohra, M., and C. Millot (1995), Hydrodynamics of an open sea Algerian eddy, *Deep Sea Res., Part I*, *42*(10), 1831–1847.

Beuvier, J., K. Beranger, C. Lebeaupin Brossier, S. Somot, F. Sevault, Y. Drillet, R. Bourdalle-Badie, N. Ferry, and F. Lyard (2012a), Spreading of the western Mediterranean deep water after winter 2005: Time scales and deep cyclone transport, *J. Geophys. Res.*, *117*, C07022, doi: 10.1029/2011JC007679.

Beuvier, J., et al. (2012b), Med12, oceanic component for the modeling of the regional Mediterranean earth system, *Mercator Ocean Q. Newsl.*, *46*, 60–66.

Bouffard, J., A. Pascual, S. Ruiz, Y. Faugère, and J. Tintoré (2010), Coastal and mesoscale dynamics characterization using altimetry and gliders: A case study in the Balearic Sea, *J. Geophys. Res.*, *115*, C10029, doi:10.1029/2009JC006087.

Bouffard, J., L. Renault, S. Ruiz, A. Pascual, C. Dufau, and J. Tintoré (2012), Sub-surface small-scale eddy dynamics from multi-sensor observations and modeling, *Prog. Oceanogr.*, *106*, 62–79.

Bouffard, J., F. Nencioli, R. Escudier, A. M. Doglioli, A. A. Petrenko, A. Pascual, P.-M. Poulain, and D. Elhmaidi (2014), Lagrangian analysis of satellite-derived currents: Application to the north western Mediterranean coastal dynamics, *Adv. Space Res.*, *53*(5), 788–801.

Chelton, D. B., R. A. Deszoeke, M. G. Schlax, K. El Naggar, and N. Siwertz (1998), Geographical variability of the first baroclinic Rossby radius of deformation, *J. Phys. Oceanogr.*, *28*(3), 433–460.

Chelton, D. B., M. G. Schlax, R. M. Samelson, and R. A. de Szoeke (2007), Global observations of large oceanic eddies, *Geophys. Res. Lett.*, *34*, L15606, doi:10.1029/2007GL030812.

Chelton, D. B., M. G. Schlax, and R. M. Samelson (2011a), Global observations of nonlinear mesoscale eddies, *Prog. Oceanogr.*, *91*(2), 167–216.

Chelton, D. B., P. Gaube, M. G. Schlax, J. J. Early, and R. M. Samelson (2011b), The influence of nonlinear mesoscale eddies on near-surface oceanic chlorophyll, *Science*, *334*(6054), 328–332.

Colas, F., J. C. McWilliams, X. Capet, and J. Kurian (2012), Heat balance and eddies in the peru-chile current system, *Clim. Dyn.*, *39*(1-2), 509–529.

Criado-Aldeanueva, F., F. J. Soto-Navarro, and J. García-Lafuente (2012), Seasonal and interannual variability of surface heat and freshwater fluxes in the Mediterranean Sea: Budgets and exchange through the strait of gibraltar, *Int. J. Climatol.*, *32*(2), 286–302.

Dai, A., T. Qian, K. E. Trenberth, and J. D. Milliman (2009), Changes in continental freshwater discharge from 1948 to 2004, *J. Clim.*, *22*(10), 2773–2792.

Debreu, L., P. Marchesiello, P. Penven, and G. Cambon (2012), Two-way nesting in split-explicit ocean models: Algorithms, implementation and validation, *Ocean Modell.*, *49*, 1–21.

Dussurget, R., F. Birol, R. Morrow, and P. D. Mey (2011), Fine resolution altimetry data for a regional application in the bay of biscay, *Mar. Geod.*, *34*(3-4), 447–476.

Eden, C., and H. Dietze (2009), Effects of mesoscale eddy/wind interactions on biological new production and eddy kinetic energy, *J. Geophys. Res.*, *114*, C05023, doi:10.1029/2008JC005129.

Escudier, R. (2015), Mesoscale eddies in the western Mediterranean Sea: Characterization and understanding from satellite observations and model simulations, PhD thesis, Univ. de les Illes Balears, Palma, Majorca, Spain.

Escudier, R., J. Bouffard, A. Pascual, P.-M. Poulain, and M.-I. Pujol (2013), Improvement of coastal and mesoscale observation from space: Application to the northwestern Mediterranean Sea, *Geophys. Res. Lett.*, *40*, 2148–2153, doi:10.1002/grl.50324.

Fairall, C., E. F. Bradley, J. Hare, A. Grachev, and J. Edson (2003), Bulk parameterization of air-sea fluxes: Updates and verification for the coare algorithm, *J. Clim.*, *16*(4), 571–591.

Feng, M., L. J. Majewski, C. Fandry, and A. M. Waite (2007), Characteristics of two counter-rotating eddies in the Leeuwin current system off the western Australian coast, *Deep Sea Res., Part II*, *54*(8), 961–980.

Font, J., J. Salat, and J. Tintoré (1988), Permanent features of the circulation in the catalan sea, *Oceanol. Acta*, *9*, 51–57.

Font, J., E. Garcialadona, and E. Gorriz (1995), The seasonality of mesoscale motion in the northern current of the western Mediterranean-several years of evidence, *Oceanol. Acta*, *18*(2), 207–219.

Font, J., C. Millot, J. Salas, A. Julia, and O. Chic (1998), The drift of modified Atlantic water from the Alboran sea to the eastern Mediterranean, *Sci. Mar.*, *62*(3), 211–216.

Fu, L.-L., D. Alsdorf, E. Rodriguez, R. Morrow, N. Mognard, J. Lambin, P. Vaze, and T. Lafon (2009), The swot (surface water and ocean topography) mission: Spaceborne radar interferometry for oceanographic and hydrological applications, paper presented at OCEANOBS09 Conference, Venice.

García, M., C. Millot, J. Font, and E. García-Ladona (1994), Surface circulation variability in the Balearic basin, *J. Geophys. Res.*, *99*(C2), 3285–3296.

Gaube, P., D. J. McGillicuddy, D. B. Chelton, M. J. Behrenfeld, and P. G. Strutton (2014), Regional variations in the influence of mesoscale eddies on near-surface chlorophyll, *J. Geophys. Res. Oceans*, *119*, 8195–8220, doi:10.1002/2014JC010111.

Gaube, P., D. B. Chelton, R. M. Samelson, M. G. Schlax, and L. W. ONeill (2015), Satellite observations of mesoscale eddy-induced Ekman pumping, *J. Phys. Oceanogr.*, *45*(1), 104–132.

Halo, I., B. Backeberg, P. Penven, I. Ansorge, C. Reason, and J. Ullgren (2013), Eddy properties in the mozambique channel: A comparison between observations and two numerical ocean circulation models, *Deep Sea Res., Part II*, *100*, 38–53.

Holland, W. R. (1978), The role of mesoscale eddies in the general circulation of the ocean-numerical experiments using a wind-driven quasi-geostrophic model, *J. Phys. Oceanogr.*, *8*(3), 363–392.

Hu, Z., A. Doglioli, A. Petrenko, P. Marsaleix, and I. Dekeyser (2009), Numerical simulations of eddies in the Gulf of Lion, *Ocean Modell.*, *28*(4), 203–208.

Hu, Z., A. Petrenko, A. Doglioli, and I. Dekeyser (2011), Study of a mesoscale anticyclonic eddy in the western part of the Gulf of Lion, *J. Mar. Syst.*, *88*(1), 3–11.

Isern-Fontanet, J., E. García-Ladona, and J. Font (2006), Vortices of the Mediterranean sea: An altimetric perspective, *J. Phys. Oceanogr.*, *36*(1), 87–103.

Jayne, S. R., and J. Marotzke (2002), The oceanic eddy heat transport, *J. Phys. Oceanogr.*, *32*(12), 3328–3345.

Katz, E. J. (1972), The levantine intermediate water between the strait of sicily and the strait of gibraltar, *Deep Sea Res., Oceanogr. Abstr.*, *19*, 507–520.

Large, W. G., J. C. McWilliams, and S. C. Doney (1994), Oceanic vertical mixing: A review and a model with a nonlocal boundary layer parameterization, *Rev. Geophys.*, *32*(4), 363–403.

La Violette, P. E., J. Tintoré, and J. Font (1990), The surface circulation of the Balearic Sea, *J. Geophys. Res.*, *95*(C2), 1559–1568.

Levy, M., L. Mémery, and G. Madec (1998), The onset of a bloom after deep winter convection in the northwestern Mediterranean Sea: Mesoscale process study with a primitive equation model, *J. Mar. Syst.*, *16*(1), 7–21.

Llinás, L., R. S. Pickart, J. T. Mathis, and S. L. Smith (2009), Zooplankton inside an Arctic Ocean cold-core eddy: Probable origin and fate, *Deep Sea Res., Part II*, *56*(17), 1290–1304.

Lozier, M. S. (1997), Evidence for large-scale eddy-driven gyres in the north Atlantic, *Science*, *277*(5324), 361–364, doi:10.1126/science.277.5324.361.

Mahadevan, A., E. DAsaro, C. Lee, and M. J. Perry (2012), Eddy-driven stratification initiates north Atlantic spring phytoplankton blooms, *Science*, *337*(6090), 54–58.

Malanotte-Rizzoli, P., et al. (2013), Physical forcing and physical/biochemical variability of the Mediterranean Sea: A review of unresolved issues and directions for future research, *Ocean Sci. Discuss.*, *10*(4), 1205–1280.

Marchesiello, P., J. C. McWilliams, and A. Shchepetkin (2003), Equilibrium structure and dynamics of the California current system, *J. Phys. Oceanogr.*, *33*(4), 753–783.

Marchesiello, P., X. Capet, C. Menkes, and S. C. Kennan (2011), Submesoscale dynamics in tropical instability waves, *Ocean Modell.*, *39*(1), 31–46.

Mason, E., and A. Pascual (2013), Multiscale variability in the Balearic Sea: An altimetric perspective, *J. Geophys. Res. Oceans*, *118*, 3007–3025, doi:10.1002/jgrc.20234.

McWilliams, J. C., and G. R. Flierl (1979), On the evolution of isolated, nonlinear vortices, *J. Phys. Oceanogr.*, *9*(6), 1155–1182.

Millot, C. (1982), Analysis of upwelling in the Gulf of Lions, in *Hydrodynamics of Semi-Enclosed Sea*, Elsevier Amsterdam, pp. 143–154.

Millot, C., M. Benzohra, and I. Taupier-Letage (1997), Circulation off Algeria inferred from the mediprod-5 current meters, *Deep Sea Res., Part I*, *44*(9), 1467–1495.

Mkhinini, N., A. L. S. Coimbra, A. Stegner, T. Arsouze, I. Taupier-Letage, and K. Béranger (2014), Long-lived mesoscale eddies in the eastern Mediterranean Sea: Analysis of 20 years of aviso geostrophic velocities, *J. Geophys. Res. Oceans*, *119*, 8603–8626, doi:10.1002/2014JC010176.

Nencioli, F., C. Dong, T. Dickey, L. Washburn, and J. C. McWilliams (2010), A vector geometry-based eddy detection algorithm and its application to a high-resolution numerical model product and high-frequency radar surface velocities in the southern California bight, *J. Atmos. Oceanic Technol.*, *27*(3), 564–579.

Okubo, A. (1970), Horizontal dispersion of floatable particles in the vicinity of velocity singularities such as convergences, *Deep Sea Res. Oceanogr. Abstr.*, *17*, 445–454.

Olita, A., A. Ribotti, R. Sorgente, L. Fazioli, and A. Perilli (2011), Sla–chlorophyll-a variability and covariability in the Algero-Provençal basin (1997–2007) through combined use of EOF and wavelet analysis of satellite data, *Ocean Dyn.*, *61*(1), 89–102.

Oschlies, A., and V. Garçon (1998), Eddy-induced enhancement of primary production in a model of the North Atlantic Ocean, *Nature*, *394*(6690), 266–269.

Pascual, A., B. B. Nardelli, G. Larnicol, M. Emelianov, and D. Gomis (2002), A case of an intense anticyclonic eddy in the Balearic Sea (western Mediterranean), *J. Geophys. Res.*, *107*(C11), 3183, doi:10.1029/2001JC000913.

Pascual, A., M.-I. Pujol, G. Larnicol, P.-Y. Le Traon, and M.-H. Rio (2007), Mesoscale mapping capabilities of multisatellite altimeter missions: First results with real data in the Mediterranean Sea, *J. Mar. Syst.*, *65*(1-4), 190–211, doi:10.1016/j.jmarsys.2004.12.004.

Peliz, A., D. Boutov, R. Cardoso, J. Delgado, and P. M. Soares (2012), The Gulf of Cadiz-Alboran sea sub-basin: Model setup, exchange and seasonal variability, *Ocean Modell.*, *61*, 49–67.

Penven, P., V. Echevin, J. Pasapera, F. Colas, and J. Tam (2005), Average circulation, seasonal cycle, and mesoscale dynamics of the Peru current system: A modeling approach, *J. Geophys. Res.*, *110*, C10021, doi:10.1029/2005JC002945.

Pinot, J.-M., J. Tintoré, and D. Gomis (1995), Multivariate analysis of the surface circulation in the Balearic Sea, *Prog. Oceanogr.*, *36*(4), 343–376.

Pinot, J.-M., J. López-Jurado, and M. Riera (2002), The Canales experiment (1996-1998). Interannual, seasonal, and mesoscale variability of the circulation in the Balearic channels, *Prog. Oceanogr.*, *55*(3), 335–370.

Poulain, P.-M., M. Menna, and E. Mauri (2012), Surface geostrophic circulation of the Mediterranean Sea derived from drifter and satellite altimeter data, *J. Phys. Oceanogr.*, *42*(6), 973–990, doi:10.1175/JPO-D-11-0159.1.

Puillat, I., I. Taupier-Letage, and C. Millot (2002), Algerian Eddies lifetime can near 3 years, *J. Mar. Syst.*, *31*(4), 245–259.

Pujol, M.-I., and G. Larnicol (2005), Mediterranean sea eddy kinetic energy variability from 11 years of altimetric data, *J. Mar. Syst.*, *58*(3-4), 121–142, doi:10.1016/j.jmarsys.2005.07.005.

Renault, L., T. Oguz, A. Pascual, G. Vizoso, and J. Tintoré (2012), Surface circulation in the Alborán Sea (western Mediterranean) inferred from remotely sensed data, *J. Geophys. Res.*, *117*, C08009, doi:10.1029/2011JC007659.

Renault, L., M. J. Molemaker, J. C. Mcwilliams, A. F. Shchepetkin, F. Lemarié, D. Chelton, S. Illig, and A. Hall (2016), Modulation of Wind-Work by Oceanic Current Interaction with the Atmosphere, *J. Phys. Oceanogr*, doi:10.1175/JPO-D-15-0232.1.

Rio, M.-H., A. Pascual, P.-M. Poulain, M. Menna, B. Barceló, and J. Tintoré (2014), Computation of a new mean dynamic topography for the Mediterranean Sea from model outputs, altimeter measurements and oceanographic in-situ data, *Ocean Sci. Discuss.*, *11*(1), 655–692.

Robinson, A. R., W. G. Leslie, A. Theocharis, and A. Lascaratos (2001), Mediterranean sea circulation, *Ocean Currents: A Derivative of the Encyclopedia of Ocean Sciences*, Academic Press, pp. 1689–1705.

Rubio, A., B. Barnier, G. Jordá, M. Espino, and P. Marsaleix (2009), Origin and dynamics of mesoscale eddies in the Catalan Sea (nw Mediterranean): Insight from a numerical model study, *J. Geophys. Res.*, *114*, C06009, doi:10.1029/2007JC004245.

Ruiz, S., J. Font, M. Emelianov, J. Isern-Fontanet, C. Millot, J. Salas, and I. Taupier-Letage (2002), Deep structure of an open sea eddy in the Algerian basin, *J. Mar. Syst.*, *33*, 179–195.

Ruiz, S., A. Pascual, B. Garau, Y. Faugière, A. Alvarez, and J. Tintoré (2009), Mesoscale dynamics of the Balearic front, integrating glider, ship and satellite data, *J. Mar. Syst.*, *78*, S3–S16, doi:10.1016/j.jmarsys.2009.01.007.

Saha, S., et al. (2010), The NCEP climate forecast system reanalysis, *Bull. Am. Meteorol. Soc.*, *91*(8), 1015–1057.

Samelson, R., M. Schlax, and D. Chelton (2014), Randomness, symmetry, and scaling of mesoscale eddy life cycles, *J. Phys. Oceanogr.*, *44*(3), 1012–1029.

Sanz, J. L. (1991), *Prospección Geofísica del Estrecho de Gibraltar: Resultados del Programa Hércules (1980-1983)*, vol. 7, Minist. de Agric., Pesca y Alimentación, Secr. Gen. Técnica.

Shchepetkin, A. F., and J. C. McWilliams (2005), The regional oceanic modeling system (ROMS): A split-explicit, free-surface, topography-following-coordinate oceanic model, *Ocean Modell.*, *9*(4), 347–404, doi:10.1016/j.ocemod.2004.08.002.

Shchepetkin, A. F., and J. C. McWilliams (2009), Correction and commentary for "ocean forecasting in terrain-following coordinates: Formulation and skill assessment of the regional ocean modeling system" by Haidvogel et al., J. Comp. Phys., 227, pp. 3595-3624, *J. Comput. Phys.*, *228*(24), 8985–9000, doi:10.1016/j.jcp.2009.09.002.

Smith, W. H. F., and D. T. Sandwell (1997), Global sea floor topography from satellite altimetry and ship depth soundings, *Science*, *277*(5334), 1956–1962, doi:10.1126/science.277.5334.1956.

Testor, P., U. Send, J.-C. Gascard, C. Millot, I. Taupier-Letage, and K. Beranger (2005), The mean circulation of the southwestern Mediterranean Sea: Algerian gyres, *J. Geophys. Res.*, *110*, C11017, doi:10.1029/2004JC002861.

Weiss, J. (1991), The dynamics of enstrophy transfer in two-dimensional hydrodynamics, *Physica D*, *48*(2), 273–294.

Wunsch, C. (1999), Where do ocean eddy heat fluxes matter?, *J. Geophys. Res.*, *104*(C6), 13,235–13,249, doi:10.1029/1999JC900062.

Erratum

In the originally published version of this article, Figure 1 did not properly cite *Millot* [1999]. This has since been corrected and this version may be considered the authoritative version of record.